



# Ultrafast ion transport at a cathode–electrolyte interface and its strong dependence on salt solvation

Bohua Wen<sup>1</sup>, Zhi Deng<sup>2</sup>, Ping-Chun Tsai<sup>1</sup>, Zachary W. Lebens-Higgins<sup>3</sup>, Louis F. J. Piper<sup>3</sup>, Shyue Ping Ong<sup>2</sup> and Yet-Ming Chiang<sup>1</sup>✉

**To access the full performance potential of advanced batteries, electrodes and electrolytes must be designed to facilitate ion transport at all applicable length scales. Here, we perform electrodynamic measurements on single electrode particles of ~6 nAh capacity, decouple bulk and interfacial transport from other pathways and show that Li intercalation into LiNi<sub>0.33</sub>Mn<sub>0.33</sub>Co<sub>0.33</sub>O<sub>2</sub> (NMC333) is primarily impeded by interfacial kinetics when using a conventional LiPF<sub>6</sub> salt. Electrolytes containing LiTFSI salt, with or without LiPF<sub>6</sub>, exhibit about 100-fold higher exchange current density under otherwise identical conditions. This anion group effect is explained using molecular dynamics simulations to identify preferred solvation structures, density functional theory calculations of their binding energies and Raman spectroscopy confirmation of solvation structure. We show that TFSI<sup>-</sup> preferentially solvates Li<sup>+</sup> compared to PF<sub>6</sub><sup>-</sup>, and yet its preferred solvation structures provide a lower Li<sup>+</sup> binding energy, suggesting a lower desolvation energy consistent with ultrafast interfacial kinetics.**

Lithium-ion battery technology today holds a dominant role in energy storage for portable devices, electrical vehicles and short-duration grid energy storage. These markets demand continued improvement in energy density, while emerging applications such as electric aviation will also require sustained high power discharge at still higher specific energy<sup>1</sup>. The historical tradeoff between energy and power in batteries is inherently due to transport limitations, which exist at a variety of length scales. In typical porous electrodes, transport limitations can include inadequate ion transport percolation in the electrolyte-filled porosity, electronic conductivity of the active materials or composite electrode or charge transfer at the electrode–electrolyte interface<sup>2,3</sup>.

Unusually fast reaction kinetics have recently been observed in certain electrolyte compositions using established intercalation compounds. Aqueous electrolytes with high salt concentrations (and thus with high viscosity and comparable ionic conductivity) exhibit up to 4.5 C rate performance in LiMn<sub>2</sub>O<sub>4</sub>|Mo<sub>6</sub>S<sub>8</sub> full cells<sup>4</sup>. Acetonitrile-based electrolytes with high salt concentrations allow ultrafast charging in graphite|lithium half cells compared to commercial carbonate electrolyte<sup>5–7</sup>. Carbonate-based electrolyte with 0.05 M LiPF<sub>6</sub> (lithium hexafluorophosphate) and 1 M LiTFSI–LiBOB (lithium bis(trifluoromethanesulfonyl)imide)—lithium bis(oxalato)borate dual-salt exhibit fast kinetics in NMC|lithium half cells<sup>8</sup>. These examples show that electrode kinetics can depend strongly on the choice of electrolyte, and in some cases can be improved even while the electrolyte conductivity is lowered, suggesting interfacial charge-transfer limitations<sup>9</sup>. In LiNi<sub>0.80</sub>Co<sub>0.15</sub>Al<sub>0.05</sub>O<sub>2</sub> (NCA) and NMC333, our group previously measured the bulk lithium diffusivity in monolithic dense samples that are free of typical binders and conductive carbon additives as well as microstructural effects<sup>10,11</sup>. These measurements showed that bulk Li diffusion should allow much more

rapid charge/discharge rate than is typically observed, again consistent with interfacial charge-transfer limitations<sup>12</sup>.

In the present work, we separate bulk and interfacial transport coefficients at the level of single cathode particles of ~28 μm diameter and ~6 nAh lithium storage capacity, using a recently developed microscopic electrodynamic measurement technique<sup>13–15</sup>. Taking NMC333 as a model cathode and investigating electrolytes that contain varying concentrations of LiPF<sub>6</sub> and LiTFSI in a common carbonate solvent (dimethyl carbonate, DMC), the role of the PF<sub>6</sub><sup>-</sup> or TFSI<sup>-</sup> anion group on interfacial charge-transfer kinetics is characterized over a wide range of cathode state of charge (SOC) (up to ~90%, corresponding to an open circuit voltage (OCV) of 4.5 V versus Li<sup>0</sup>). We show that the exchange current density for electrolytes containing 1 to 5 M TFSI<sup>-</sup> can be raised nearly 100-fold compared to those containing only PF<sub>6</sub><sup>-</sup>. To explain this behaviour, we elucidate the preferred configurations of the respective anion groups in the first Li<sup>+</sup> solvation shell using molecular dynamics (MD) simulations and find that differences in density functional theory (DFT) binding energy are responsible for the observed vast differences in charge-transfer reaction rates. These effects, observed at the single-particle level, are further shown to translate to macroscopic NMC333 electrodes using the same electrolytes, wherein large differences in discharge capacities at high current rates (for example, 3–4 times higher capacity at 10 C) are demonstrated. These results show that electrolytes can be specifically tailored to optimize interfacial charge transfer, and therefore capacity use at high rates, as is needed for many emerging applications.

## Single-particle electrode measurements of interfacial kinetics

Our three-electrode single-particle electrochemical cell technique, which leverages previous developments<sup>14</sup>, uses electrodynamic

<sup>1</sup>Department of Materials Science and Engineering, Massachusetts Institute of Technology, Cambridge, MA, USA. <sup>2</sup>Department of NanoEngineering, University of California San Diego, La Jolla, CA, USA. <sup>3</sup>Department of Physics, Applied Physics and Astronomy, Binghamton University, Binghamton, NY, USA. ✉e-mail: [ychiang@mit.edu](mailto:ychiang@mit.edu)

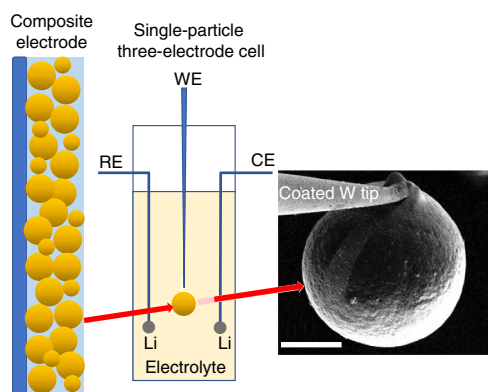


**Fig. 1 | Design of experiments.** Single particles are isolated from commercial NMC powder normally used in composite electrodes, and measured in a three-electrode cell. An scanning electron microscope image of a 28  $\mu\text{m}$  particle mounted on a tungsten probe is shown in the inset. Scale bar, 10  $\mu\text{m}$ .

protocols and analysis that allow us to separate bulk and interfacial transport and, specifically, to measure the exchange current density,  $j_0$ , at the solid–liquid electrolyte interface (Fig. 1)<sup>13</sup>. We aimed to reveal electrolyte composition and SOC effects on  $j_0$  that would provide insights on how to design a system for fast interfacial kinetics. A series of model electrolyte compositions were evaluated, each using DMC solvent various concentrations of a single lithium salt ( $\text{LiPF}_6$  at 1, 1.5 and 2 M concentrations, or LiTFSI at 3, 4 and 5 M concentrations), as well as dual-salt mixtures of  $\text{LiPF}_6$  and LiTFSI (in a 1:1 molar ratio). The salt concentration ranges were chosen on the basis of the following constraints:  $\text{LiPF}_6$  has limited solubility in DMC (saturation at 2 M), while pure LiTFSI electrolytes are unstable at low concentrations and high potentials ( $\sim 4.5$  V versus  $\text{Li}/\text{Li}^+$ ).

Supplementary Fig. 1 shows typical voltage versus capacity curves during galvanostatic charge at a 1/20 C rate to an upper voltage cutoff of 4.55 V for the single-particle electrodes. After galvanostatic charging, micro-electrochemical impedance spectroscopy (EIS) and potentiostatic intermittent titration tests (PITT) were performed on the single-particle electrodes at selected SOC values, from which the exchange current density,  $j_0$ , was obtained as a function of SOC. In addition, PITT was used to obtain the electrochemical Biot number ( $B$ ), which characterizes the ratio of bulk to interfacial transport resistance, following procedures explained in ref. <sup>13</sup> and Supplementary Methods.

Results are first shown for the dependence of  $j_0$  on three independent variables: SOC, salt species and total salt concentration. In the reference electrolyte, which contains 1 M  $\text{LiPF}_6$ , (Fig. 2a,c), the  $j_0$  values measured by EIS and PITT on two particles (nos. 1 and 2 in Supplementary Table 1) show an SOC dependence that is in good agreement with our previous work<sup>13</sup>. The  $j_0$  increases by a factor of  $\sim 10^2$  with increasing charge voltage (delithiation) and approaches  $\sim 0.2$   $\text{mA cm}^{-2}$  at high voltage ( $\sim 4.5$  V); the  $j_0$  is also largely reversible between charge and discharge. Using NMC333 at a voltage cutoff of 4.5 V minimizes micro-cracking of the secondary particles upon cycling, compared to, for example, NCA<sup>13</sup>. Such micro-cracking can introduce notable errors in surface area estimation. In PITT, errors in the value of  $j_0$  derive primarily from the accuracy of input value  $dU/dC$ , the derivative of the equilibrium potential,  $U$ , with respect to Li concentration,  $C$ , and the time/current measurement resolution in the micro-scale experiments. We analyse both EIS and PITT results for  $j_0$  and obtain closely agreeing results.

Compared to the baseline 1 M electrolyte,  $j_0$  for 1.5 and 2 M  $\text{LiPF}_6$  concentration displays a similar SOC dependence, with  $j_0$  increasing by over an order of magnitude between OCV of 3.6 and 4.6 V

(Fig. 2a). With increasing  $\text{LiPF}_6$  concentration,  $j_0$  systematically decreases, to values about a factor of three lower. In contrast, electrolytes containing 3 to 5 M LiTFSI show both higher and nearly SOC-independent  $j_0$  (due to limited electrochemical stability, seen in Supplementary Fig. 2, LiTFSI-only electrolytes had salt concentrations  $> 3$  M). Compared to the electrolytes containing  $\text{LiPF}_6$  salt,  $j_0$  is about  $10^2$  higher at the lower end of the OCV range. The strong anion dependence of interfacial kinetics is further evidenced in dual-salt electrolytes, Fig. 2b, for which lower LiTFSI concentrations are electrochemically stable (see Supplementary Fig. 2). Even at lower LiTFSI concentration,  $j_0$  for the dual-salt electrolyte is a factor of 10 to 100 greater than the 1 M  $\text{LiPF}_6$  base case.

To obtain  $j_0$  in a d.c. mode for comparison with the EIS results, PITT measurements were carried out, each on a separate  $\sim 28$ - $\mu\text{m}$ -diameter particle (see Fig. 2c and Supplementary Table 1). Supplementary Fig. 3 shows that these data follow an expected  $1/t^{1/2}$  dependence. The marked difference in kinetics between electrolytes is clear; there is 3–4 times higher current at the same potential for the electrolyte containing 1 M  $\text{LiPF}_6$  + 1 M LiTFSI, compared to two electrolytes containing  $\text{LiPF}_6$  alone. The PITT-obtained  $j_0$  values taken across the entire OCV range, Fig. 2d, agree closely with the EIS-obtained values (Fig. 2a,b). Together, these results show that  $j_0$  as high as 3  $\text{mA cm}^{-2}$  can be reached using LiTFSI; including past results<sup>13</sup>, these are high exchange current densities for a Li-ion system.

The PITT data were also analysed to obtain the electrochemical Biot number,  $B$ , to evaluate the relative contributions of interfacial and bulk resistance to Li transport in the present NMC333 with these electrolytes. Based on the numerical value of  $B$ , the kinetics are: (1) interfacial reaction control ( $B < 10^{-1}$ ); (2) mixed control ( $10^{-1} < B < 10^1$ ) and (3) diffusion control ( $B > 10^1$ )<sup>13,16,17</sup>. Figure 3a shows  $B$  versus OCV for the three PITT measurements in Fig. 2, and the inset in Fig. 3b illustrates the spatial distribution of Li concentration within particles for low and high  $B$ , respectively. Notably, for the electrolyte containing 1 M  $\text{LiPF}_6$  + 1 M LiTFSI,  $B$  exceeds 100 over virtually the entire OCV range, showing that  $j_0$  is high enough that interfacial charge transfer is no longer rate limiting (at this particle size). In contrast, the two  $\text{LiPF}_6$  electrolytes yield  $B$  values in the 1–30 range, and at lower OCV have mixed control with substantial resistance arising from interfacial kinetics.

These results reveal, in a Li-ion system, the direct impact of an anion group on microscopic interfacial kinetics. Figure 3b summarizes all the measured  $j_0$  values for the present electrolytes, at an OCV of 4.5 V (which corresponds to  $\sim 90\%$  SOC for NMC333). The interfacial reaction rate when TFSI<sup>-</sup> is the anion group is at least one order of magnitude higher than for PF<sub>6</sub><sup>-</sup> at the same concentration. The TFSI<sup>-</sup> results are striking for having little concentration dependence between 1 and 5 M, whereas the PF<sub>6</sub><sup>-</sup> results decrease steeply with increasing concentration. The solvation energetics underlying these trends are explored later in this manuscript.

## Results in macroscopic electrodes

If our interpretation of the single-particle results is correct, the observed differences in kinetics should translate to cells using macroscopic electrode coatings as well. Three electrolytes, DMC with 1 M  $\text{LiPF}_6$ , 1 M  $\text{LiPF}_6$  + 1 M LiTFSI and 1 M  $\text{LiPF}_6$  + 2 M LiTFSI were tested with NMC333 composite cathodes (coated on aluminium foil current collectors) and Li metal counter electrodes in coin cells and three-electrode Swagelok-type cells (see Methods). In the dual-salt cases, the 1 and 2 M LiTFSI concentrations are stable with the aluminium current collector due to the passivation provided by the  $\text{LiPF}_6$ . Coin cell results are shown in Fig. 4a, and three-electrode Swagelok cell results in Fig. 4b. For C rates up to 2 C, the differences between the three electrolytes are minor; at 1/10 C, the NMC333 specific capacity between 2.5–4.5 V is  $\sim 185$   $\text{mAh g}^{-1}$ , corresponding to about 85% of the theoretical capacity. However, at 5 and 10 C rates, large differences in discharge capacity are observed, with

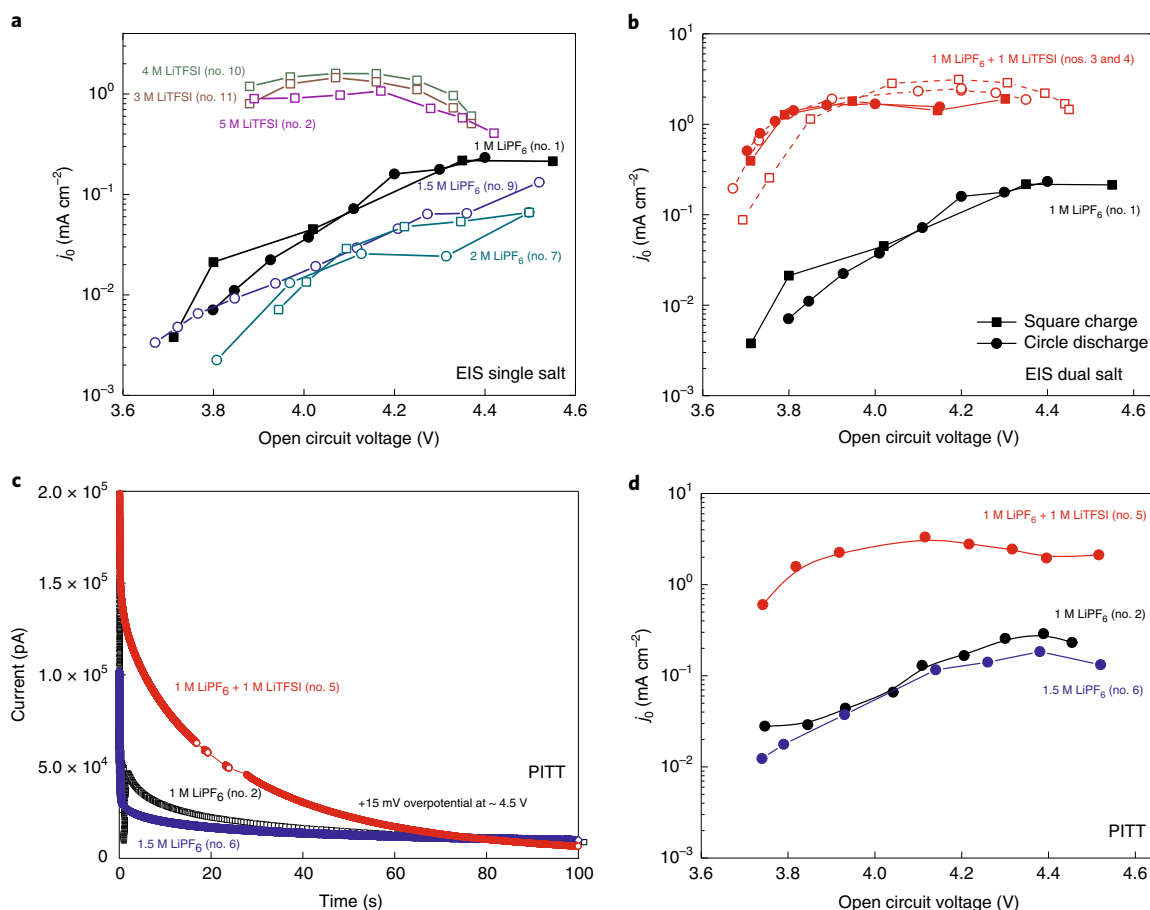


**Fig. 2 | Kinetics investigation of NMC333 single-particle electrodes in liquid electrolytes using EIS and PITT measurements.** **a, b**,  $j_0$  of NMC333 as a function of SOC from EIS in single-salt electrolytes: LiPF<sub>6</sub> (1, 1.5 and 2 M), and LiTFSI (3, 4 and 5 M) electrolytes (**a**) and dual-salt mixture (1 M LiPF<sub>6</sub> + 1 M LiTFSI) electrolytes compared to 1 M LiPF<sub>6</sub> (**b**). **c**, PITT current-time profiles ( $t < 100$  s) of single-particle electrodes at high-voltage region ( $\sim -4.5$  V) with +15 mV overpotential in 1 M LiPF<sub>6</sub>, 1.5 M LiPF<sub>6</sub> and dual-salt 1 M LiPF<sub>6</sub> + 1 M LiTFSI electrolytes. Current spikes due to instrumental switching for the red curve at 18–28 s have been removed. **d**,  $j_0$  of the selected electrolytes from PITT measurements. In **a**, **b** and **d**, square and round symbols correspond to data obtained on charge and discharge, respectively, and numbers provided for each data set correspond to individual particles for which specifications are given in Supplementary Table 1.

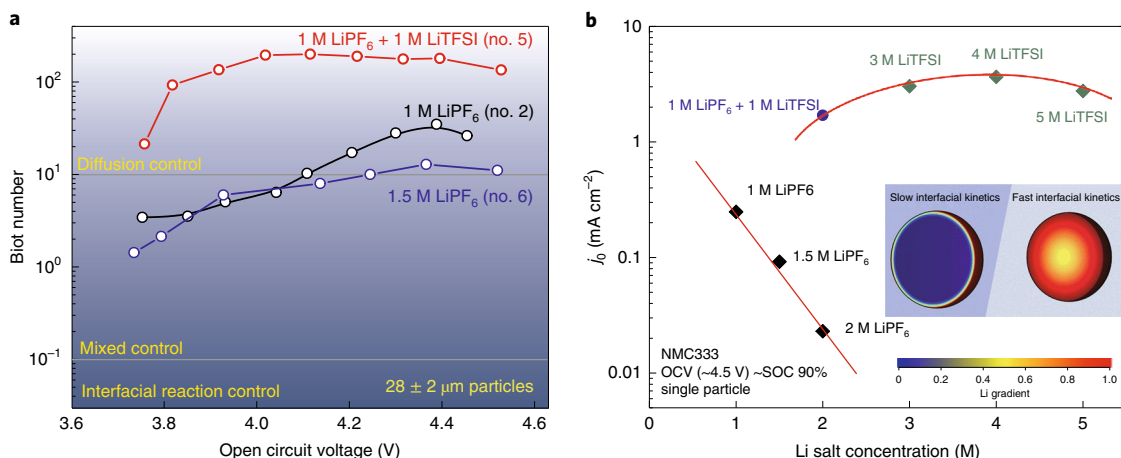


**Fig. 3 | Kinetic limitations for NMC333 as a function of interfacial reaction rate.** **a**, The electrochemical Biot number ( $B$ ) for  $28 (\pm 2) \mu\text{m}$  NMC333 particles obtained from PITT, plotted against cell OCV, for electrolytes containing 1 M LiPF<sub>6</sub>, 1.5 M LiPF<sub>6</sub> and 1 M LiPF<sub>6</sub> + 1 M LiTFSI, each in DMC. The blue gradient illustrates the transition in rate limitation across three regimes: (1) interfacial reaction control ( $B < 10^{-1}$ ); (2) mixed control ( $10^{-1} < B < 10^1$ ) and (3) diffusion control ( $B > 10^1$ ). **b**, Map of  $j_0$  at high voltage ( $\sim -4.5$  V) for all electrolytes tested; lines are guides for the eye. Inset illustrates spatial distribution of Li within a cathode particle for cases of low and high  $j_0$ .

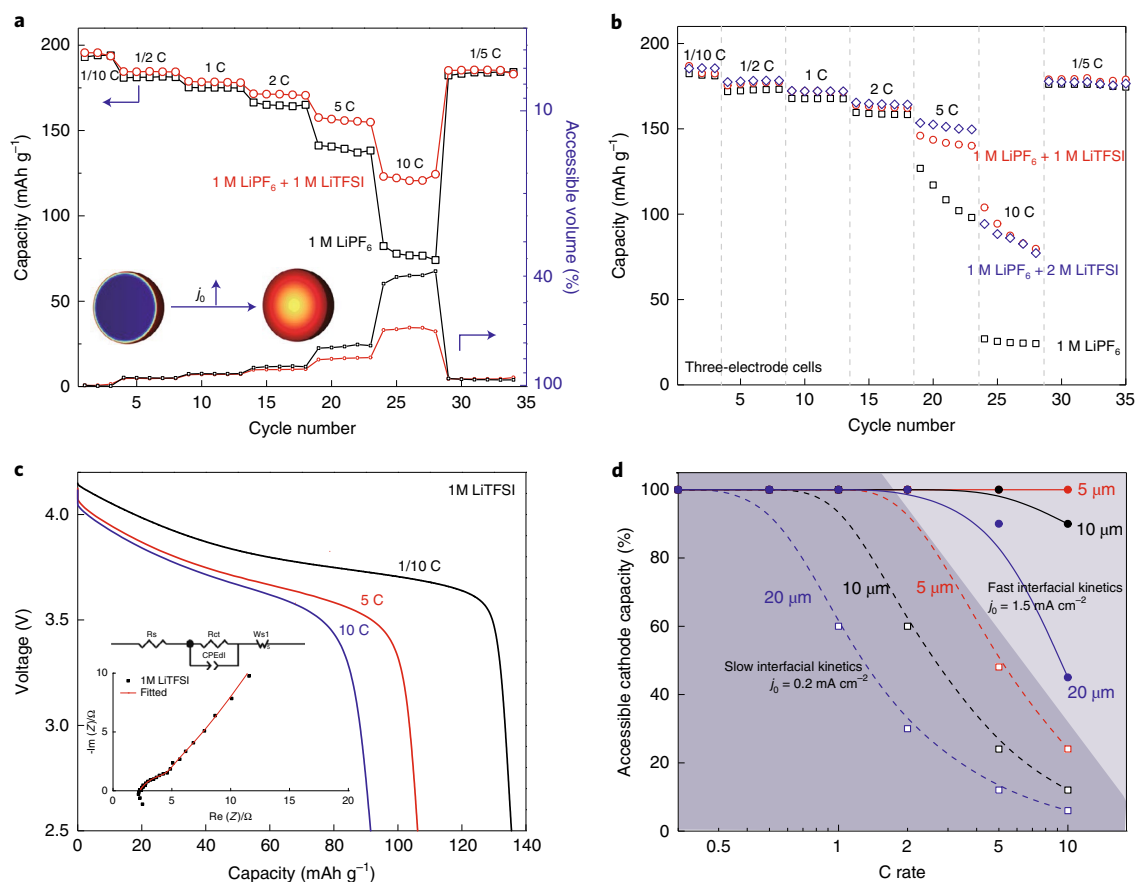


**Fig. 4 | Macroscopic kinetics of NMC333 composite electrodes in selected electrolytes.** **a**, Specific capacity measured in coin cells in electrolytes containing 1 M LiPF<sub>6</sub> and dual-salt with 1 M LiTFSI, versus cycle number. Materials use is also shown, plotted as accessible volume in a spherical particle. **b**, Three-electrode cells tested with selected electrolytes. Cells are charged at 1/3 C rate to 4.5 V followed by subsequent increasing discharge rates to 2.5 V (1 C = 2 mA cm<sup>-2</sup>). **c**, Voltage versus capacity for NMC333 cast on Pt-sputtered current collector in 1 M LiTFSI, measured between 2.5 to 4.15 V; Inset: Nyquist plot for three-electrode Swagelok cells in DMC + 1 M LiTFSI electrolyte, taken after 40 cycles, along with a schematic of the equivalent electrical circuit that was fit to the data. **d**, The accessible capacity as a function of C rate for commercially relevant NMC particle sizes of 5, 10 and 20 μm, when ‘slow’ (light blue regime) and ‘fast’ (dark blue regime) interfacial kinetics are available.

electrolyte containing LiTFSI yielding nearly twice the capacity at 10 C in the coin cells and nearly three times the capacity at 10 C in the Swagelok type cells, compared to LiPF<sub>6</sub>-only electrolyte. In the coin cells, the electrolyte containing LiTFSI salt yielded ~70% of the 1/10 C capacity at 10 C (Fig. 4a).

The three-electrode cell configuration also allows separation of the charge-transfer resistance contributions of the cathode and the Li metal electrode. Here, we used DMC + 1 M LiTFSI as the electrolyte and circumvented the instability issue (Supplementary Fig. 2) by sputter-coating ~200 nm Pt onto the steel coin cell casing, which serves as the cathode current collector. The electrochemical measurements were also limited to a lower voltage range of 2.5 to 4.15 V. As shown in Fig. 4c, these cells also show good retention of capacity at the higher C rates (138 mAh g<sup>-1</sup> at 1/10 C, 106 mAh g<sup>-1</sup> at 5 C and 92 mAh g<sup>-1</sup> at 10 C, respectively). Comparing the charge-transfer resistance,  $R_{ct}$ , for the NMC333 cathode in contact with an electrolyte with 1 M LiPF<sub>6</sub> only, and one with 1 M LiTFSI only, we obtained  $R_{ct}$  of ~67 Ω for the former and extremely low  $R_{ct}$  of ~4 Ω for the latter (Supplementary Fig. 4). (In contrast, the lithium metal interfacial resistance during metal deposition/stripping is ~10 Ω in both electrolytes.) Thus the trends observed in single-particle measurements apply to conventional coated electrodes as well.

NMC cathode powders are typically available with various particle size ranges. Given our measurements of  $j_0$  and the previous

analyses, it is possible to model the cathode use for various particle sizes in the limit where interfacial transport is rate limiting. Taking the Li<sup>+</sup> flux through the interface to be of standard Butler-Volmer form:

$$Q = A \times j_0 \times \left[ \exp\left(\frac{F}{2RT}\eta\right) - \exp\left(-\frac{F}{2RT}\eta\right) \right] \quad (1)$$

where  $Q$  has units of current,  $A$  is area ( $A = 4\pi r^2$ ),  $\eta$  is the overpotential (here assumed to be 100 mV, although it will vary with C rate and other extrinsic parameters), charge-transfer coefficient is 0.5, and  $F$ ,  $R$  and  $T$  have their usual meaning. The accessible capacity is determined from the volume fraction of the particle through which lithium transport can occur at a given time and C rate as Fig. 4d shows. Slow kinetics corresponds to  $j_0 = 0.2$  mA cm<sup>-2</sup>, representative of DMC with 1 M LiPF<sub>6</sub> (Fig. 4d), and fast kinetics corresponds to  $j_0 = 1.5$  mA cm<sup>-2</sup>, close to values we measured for DMC with 1–5 M LiTFSI. It is clear that without high  $j_0$ , high capacity use (for example, >60%) cannot be obtained at C rates of 5 or 10 C, even at relatively fine particle sizes.

#### Cathode-electrolyte interface (CEI) composition analysis

Since one possible cause of the dramatic anion group effect on interfacial transport is the formation of compositionally distinct

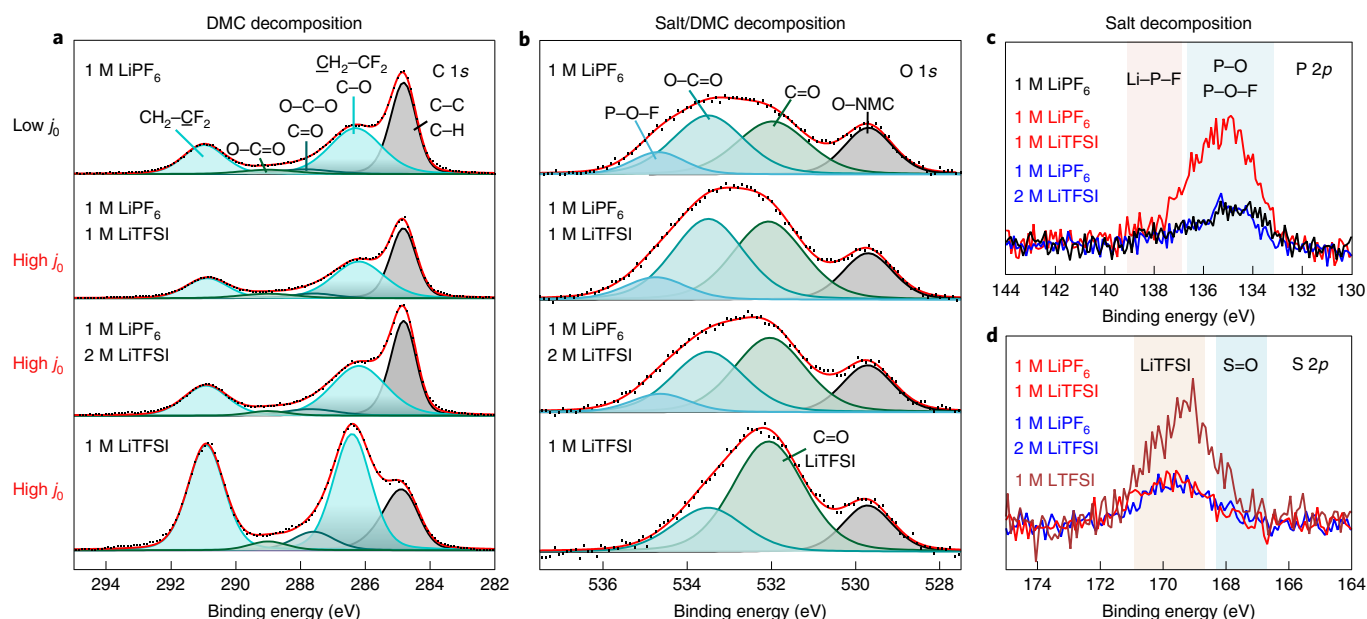


**Fig. 5 | XPS characterization of the solvent and salt interfacial compositions of cycled NMC333 composite electrodes.** **a–d**, XPS spectra of the C 1s (**a**), O 1s (**b**), P 2p (**c**) and S 2p (**d**) for cycled NMC333 with four different electrolyte salt combinations, organized in rows for the different salts according to whether they yielded low or high values of  $j_0$  and in columns according to the XPS spectral range where features would be expected for. Peak assignments are based on previous reports<sup>18–23</sup>. **a**, Shows the decomposition of the DMC solvent alone, **b** shows of the salt or DMC, and **c** and **d** of the salt alone. The C 1s and O 1s core regions (**a,b**) along with their peak fits provide a rough assignment of CEI species. The NMC333 electrodes were cycled at 0.2 mA cm<sup>-2</sup> for three formation cycles and at 2 mA cm<sup>-2</sup> for 20 cycles, respectively. All electrodes are examined after cell disassembly in the lithiated state at a potential of 3.6 V with respect to Li/Li<sup>+</sup>.

solid–electrolyte interphases (SEIs)<sup>18–20</sup>, we undertook X-ray photoelectron spectroscopy (XPS) characterization of the NMC333 particle surface after extended cycling in four selected electrolytes (Fig. 5). In the C 1s core region, the peak at 284.8 eV associated with carbon black (C–C) is used for peak calibration. The C matrix from DMC decomposition in the various salt combinations have similar spectra composed of O–C=O (289.0 eV), C=O (287.6 eV) and polyether carbon (286.5 eV, CH<sub>2</sub>O). We see no notable difference in these peaks between the electrolytes giving high and low  $j_0$ . (The higher intensity of the CH<sub>2</sub>–CF<sub>2</sub> (290.5 eV) peak associated with polyvinyl difluoride (PVDF) in the bottom row is attributed to a locally higher binder concentration.)

In the O 1s core region, Fig. 5b, the NMC lattice oxygen peak (O–NMC) is distinguishable and has comparable intensity for all electrodes. This indicates that any solvent or salt decomposition forms a CEI of <5 nm thickness. In these spectra, surface species can be assigned to C=O (532.1 eV), O–C=O (533.5 eV) and P–O–F (534.8 eV)<sup>18,20</sup>. There is a small increase in C=O with increased LiTFSI salt attributed to more DMC solvent decomposition or possibly overlapping with TFSI<sup>-</sup> decomposed species, but otherwise the four electrolytes do not vary noticeably in these features. The P–O–F peak at 534.4 eV, which is only present for LiPF<sub>6</sub> containing electrolytes, can be generated from hydrolysis of LiPF<sub>6</sub> with trace H<sub>2</sub>O in the electrolyte. Comparing the electrolytes with high  $j_0$  in the bottom three rows, there is no correlation between  $j_0$  and the presence or absence of the P–O–F peak. Comparing the spectra for the C 1s and O 1s core regions, there is no notable CEI layer compositional difference between electrolytes, unlike what has been observed in other cases including LiDFOB<sup>18</sup> or DEFP<sup>19</sup>, or coating layers, for example AlPO<sub>4</sub> (ref. 20).

Turning to the P 2p and S 2p in Fig. 5c,d, we compare the products of the breakdown of LiPF<sub>6</sub> and LiTFSI components in the concentrated electrolytes. For the LiPF<sub>6</sub> containing electrolytes, the P 2p peaks are associated with P–O or P–O–F species<sup>20</sup>, which are

common components of the CEI for LiPF<sub>6</sub> electrolytes and form through hydrolysis of LiPF<sub>6</sub> (refs. 21,22). The 1 M LiTFSI case has the strongest P–O–F peak, while the pure LiPF<sub>6</sub> and 2 M LiTFSI cases show similar intensities. The S 2p peak is assigned to LiTFSI decomposition based on previous observations<sup>22,23</sup>. LiTFSI decomposition is suppressed with the addition of LiPF<sub>6</sub> in the electrolyte. In both the P 2p and S 2p core regions, salt anion decomposition is found to depend on the salt mixture, although the intensity changes indicate only small changes in the CEI composition. Taken together, the solvent and salt decomposition species show no large electrolyte dependence between the four electrolytes tested. The F 1s, Li 1s and Mn 2p core regions and their detailed peak assignments and atomic percentages are given in Supplementary Figs. 5 and 6 to provide a detailed comparison of the surface layer composition for each electrolyte. While the F 1s and Li 1s core regions show the presence of LiF at the CEI, which scales with the concentration of P–O–F species<sup>24–28</sup>, these features also do not explain the anion dependence of the charge-transfer kinetics. Thus, we turned towards a detailed analysis of the electrolyte solvation structure.

### Simulations of solvation structures

The coordination numbers (CNs) of Li solvation structures (example shown in Fig. 6a) are determined by integrating the radial distribution function (RDF) (Fig. 6b and Supplementary Fig. 7) over the first peak. As C, P and N are uniquely contributed by DMC, PF<sub>6</sub><sup>-</sup> and TFSI<sup>-</sup>, respectively, we used the CN of these species to estimate the coordination of solvent and salt anions around each Li (Supplementary Table 2). As the concentration increases, the CN of either P or N increases since more anions coordinate Li ions in highly concentrated electrolytes. Even at the lowest concentration (1 M), the CNs corresponding to anions are already larger than 1, suggesting that at least one anion coordinates a Li ion in the solvation process. For the same molarity of a single salt (LiPF<sub>6</sub> or LiTFSI), the number of TFSI<sup>-</sup> (number of N atoms) around each Li tends to

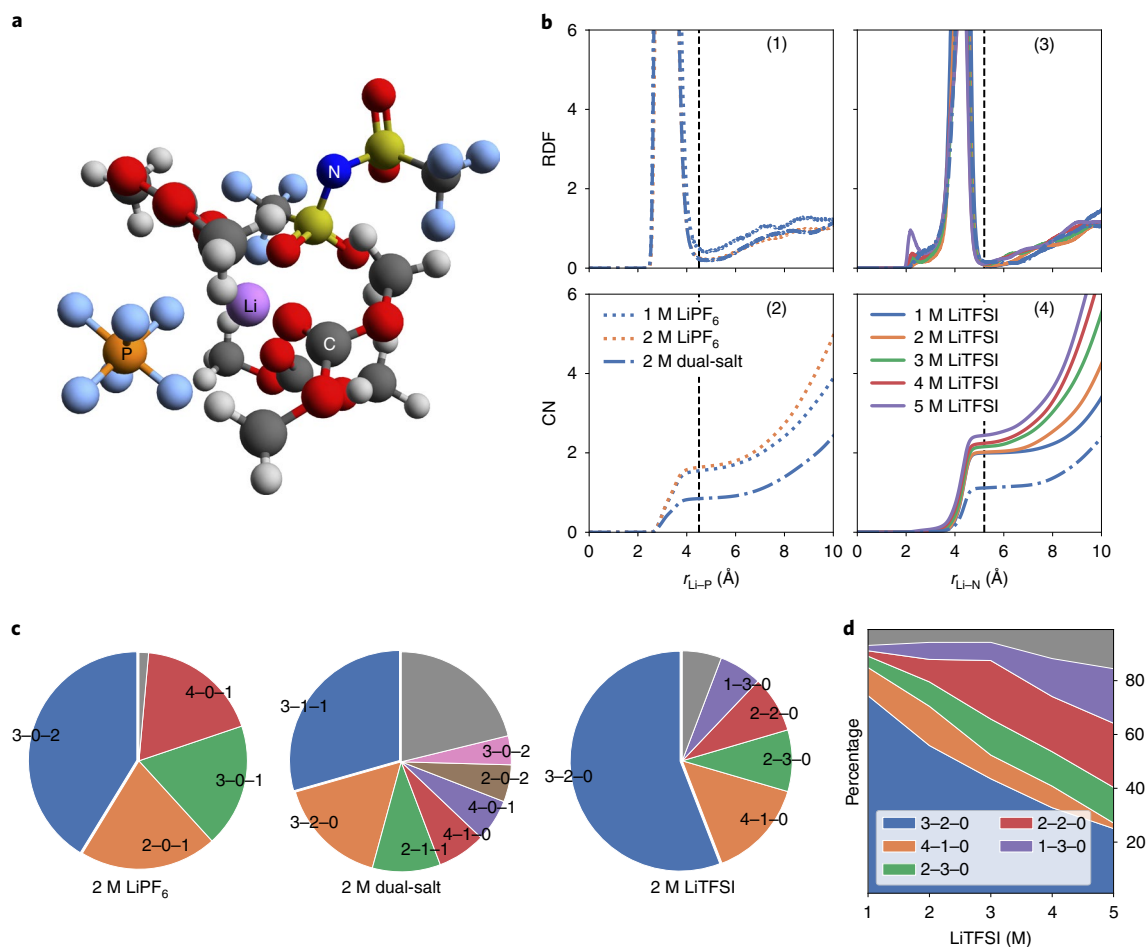


**Fig. 6 | CN and solvation structures.** **a**, An example of a 3-1-1 (3 DMC, 1 TFSI<sup>-</sup> and 1 PF<sub>6</sub><sup>-</sup>) solvation structure extracted from MD simulation of 2 M dual-salt electrolyte. Purple, Li; dark grey, C; light grey, H; red, oxygen; blue, N; light blue, F; orange, P, Li, as well as the C, N and P atoms used to determine the number of DMC, TFSI<sup>-</sup> and PF<sub>6</sub><sup>-</sup> around the Li are explicitly labelled. **b**, RDFs and integrated CNs of P (1 and 2) and N (3 and 4) around Li in different electrolytes. The vertical dashed line is the cutoff radius in calculating CNs. **c,d**, Ratio of main solvent-anion coordination environments in 2 M electrolytes (**c**) and pure LiTFSI electrolytes of various concentrations (**d**). The solvation structures are denoted as X-Y-Z, where X is the number of DMC solvent molecules, Y is the number of TFSI<sup>-</sup> and Z is the number of PF<sub>6</sub><sup>-</sup>. Other statistically insignificant solvation structures are shaded grey.

be higher than that of PF<sub>6</sub><sup>-</sup> (number of P atoms). In the equimolar dual-salt system, a larger CN for N than P is observed. Both these observations indicate a stronger tendency of TFSI<sup>-</sup> to coordinate Li ions. Figure 6c shows the distribution of the Li coordination environments for single and dual-salt systems at a total salt concentration of 2 M. It is observed that the most common solvation structure is one where Li is coordinated by three DMC solvent molecules and two anions. In the dual-salt system, the most common solvation structure is the 3-1-1 configuration, that is, three DMC, one TFSI<sup>-</sup> and one PF<sub>6</sub><sup>-</sup>, while the second most common configuration is 3-2-0. This is in agreement with the stronger tendency of TFSI<sup>-</sup> to coordinate with Li observed from the RDF analysis. Figure 6d shows the change in the ratio of main coordination environments with salt concentration in pure LiTFSI electrolytes. As the salt concentration increases, an increase in the number of environments with higher CN<sub>TFSI<sup>-</sup></sub>:CN<sub>DMC</sub> is observed. In all simulated electrolytes, less than 0.1% of Li ions are solvated by only solvent molecules, even at the lowest salt concentration (1 M). Therefore, we focus on the main solvation structures involving salt anions in our binding energy calculations.

The computed binding energies for the 2 M single-salt electrolytes (Fig. 7a) using the polarizable continuum model (PCM) are qualitatively in agreement with the distribution of observed

clusters in the MD simulations (Fig. 6c); that is, the most common 3-2-0 and 3-0-2 configurations in the single-salt LiPF<sub>6</sub> and LiTFSI electrolytes have the highest binding energies. In the 2 M dual-salt electrolyte (middle of Fig. 7a), the most common 3-1-1 configuration in the MD simulations has a binding energy of 1.7 eV, which is between that of pure TFSI<sup>-</sup> and pure PF<sub>6</sub><sup>-</sup>. That is, the replacement of PF<sub>6</sub><sup>-</sup> by TFSI<sup>-</sup> reduces the Li binding energy by ~1 eV and Li becomes less strongly bound to its solvation shell. It can also be observed that the CN of DMC solvent molecules has a relatively small effect on the Li binding energy, as can be seen from the relatively similar Li binding energies of the 3-2-0 and 2-2-0 configurations, as well as the 2-3-0 and 1-3-0 configurations. While the general trend is that the higher the binding energy, the greater the proportion of that particular configuration in the MD simulations, it is clear that the constraints imposed by the high salt concentration and packing considerations also play a role. For instance, the TFSI-rich configurations (3-2-0 and 3-1-1) dominate the 2 M dual-salt electrolyte even though the TFSI-based configurations have lower binding energies than the PF<sub>6</sub>-based configurations. This can be explained by the fact that the larger and less symmetric TFSI<sup>-</sup> can coordinate multiple Li ions via its four oxygen atoms. As shown in Supplementary Fig. 8, each TFSI<sup>-</sup> is typically coordinated by 2-3 Li<sup>+</sup> while each PF<sub>6</sub><sup>-</sup> is coordinated by 1-2 Li<sup>+</sup>. Given that the

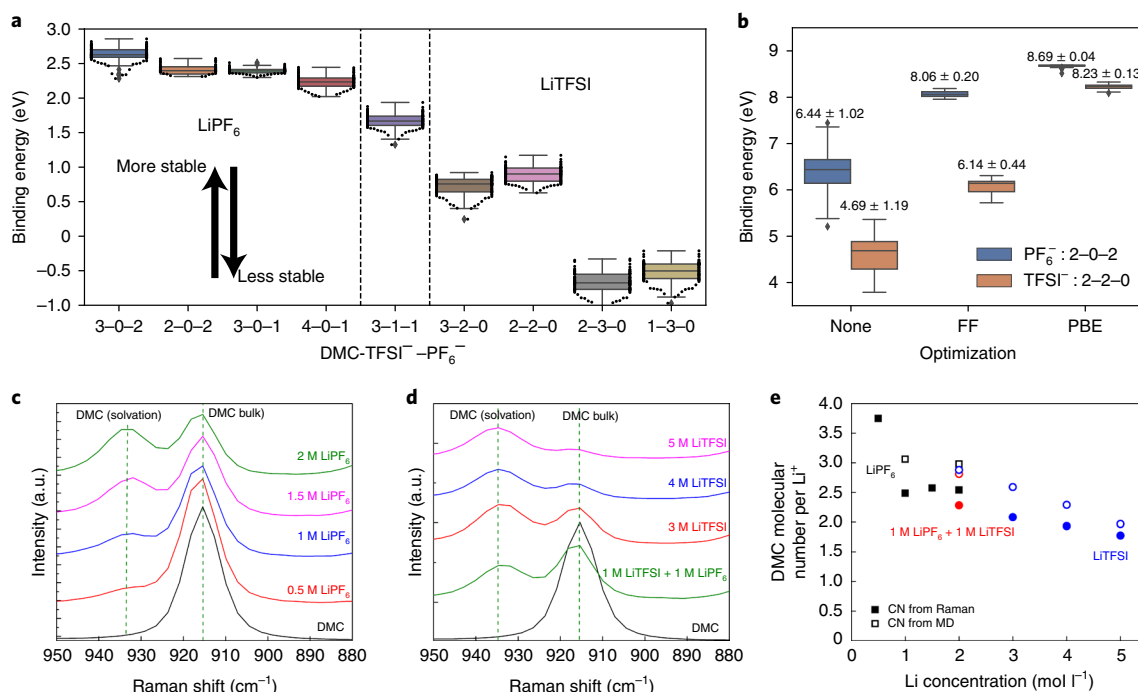


**Fig. 7 | Li binding energy and Raman spectra in various electrolytes.** **a**, DFT binding energies of the most common solvation structure clusters in 2 M electrolytes and higher concentration LiTFSI electrolytes using PCM calculations. Energies were calculated using the B3LYP<sup>38</sup> functional on extracted clusters optimized using the force field used in the MD simulations. A more positive binding energy indicates a more stable solvation structure. The chart can be divided into three parts by the vertical dashed lines, where the left, middle and right parts show the coordination environments mainly found in pure LiPF<sub>6</sub>, dual-salt and pure LiTFSI electrolytes, respectively. For each coordination environment, the energies of 100 solvation structures extracted from the MD simulations are computed using the B3LYP functional to obtain a distribution of Li binding energies. The coloured boxes indicate the interquartile range and the horizontal line in the box indicates the median Li binding energy for each environment. All data points are shown as black circles. **b**, Binding energies of 2-0-2 and 2-2-0 clusters without optimization, with force field (FF) optimization and with DFT optimization using the Perdew-Burke-Ernzerhof functional. All energies were computed using the B3LYP functional. **c–e**, Raman spectra obtained from pure DMC solvent and LiTFSI (**c**) and LiPF<sub>6</sub> containing electrolytes tested in this study (**d**) together with the estimated DMC CN per Li<sup>+</sup> (**e**), for which peak shifts resulting from the molecular interaction of PF<sub>6</sub><sup>-</sup> and TFSI<sup>-</sup> anions with DMC solvent molecules are discussed in the text.

ratio of Li<sup>+</sup> to anions is 1:1, the more packing-efficient TFSI-based solvation environments dominate.

We have also investigated the effect of different optimization methods on the gas phase binding energies, using the 2-0-2 and 2-2-0 clusters, that is, two DMC and two identical anions, as the test case (Fig. 7b). The average differences in gas phase binding energies for these two clusters are 1.75, 1.92 and 0.46 eV for the unoptimized, force-field-optimized and DFT-optimized calculations, respectively. Optimization using the force field or DFT causes a substantial relaxation of the extracted MD clusters to a more stable gas phase configuration, leading to a higher binding energy. This effect is more pronounced for the TFSI 2-2-0 configuration with DFT, possibly due to its larger size and greater flexibility compared to the PF<sub>6</sub><sup>-</sup> anion. The difference in the FF-optimized PCM binding energies is closest to the difference in the unoptimized gas phase binding energies (Supplementary Fig. 9). We believe that the FF-optimized PCM or unoptimized configurations are the closest reflection of the environment of the clusters in solution, in comparison to the optimized gas phase configurations. However, regardless of the choice of optimization method, the qualitative observation that the binding energies of Li<sup>+</sup> with TFSI<sup>-</sup> is lower than PF<sub>6</sub><sup>-</sup> holds true in all cases.

Considering all the observations, we surmise that the presence of TFSI<sup>-</sup> has two mutually reinforcing effects on Li solvation. First, TFSI<sup>-</sup> preferentially coordinates Li, even when PF<sub>6</sub><sup>-</sup> is present. Second, TFSI<sup>-</sup> decreases the binding energy of Li, resulting in more facile desolvation and more rapid kinetics in TFSI-containing

electrolytes. These effects explain why TFSI<sup>-</sup> appears to be equally effective in increasing exchange current when PF<sub>6</sub><sup>-</sup> is present or absent. As the LiTFSI concentration increases, unfavourable Li solvation environments with negative binding energies increasingly dominate (Fig. 6d). We believe that the presence of these unfavourable Li solvation environments account for the saturation of the exchange current at higher LiTFSI concentrations.

We further confirm these observations using Raman spectroscopy<sup>29,30</sup>. Solvated DMC molecules in TFSI<sup>-</sup> containing electrolytes show a higher shift ~935 cm<sup>-1</sup> compared to that in LiPF<sub>6</sub> electrolytes (Fig. 7c,d), suggesting lower binding energy for LiTFSI-DMC aggregation. We also decouple the number of solvated DMC molecules per Li<sup>+</sup> from the relative Raman peak intensities<sup>30</sup> over a wide range of salt concentrations (Supplementary Fig. 10). The lower DMC per Li<sup>+</sup> for TFSI<sup>-</sup> containing electrolytes (Fig. 7e) is consistent with the MD calculations. As the concentration of LiTFSI increases, the Li binding energies for the main solvation structures further decrease, compensating for the lower bulk ionic conductivity of the electrolyte at high salt concentrations (Supplementary Fig. 11). On the other hand, LiPF<sub>6</sub> electrolytes lack this mechanism (that is, the CNs are similar between 1 and 2 M concentration), and the electrode kinetics drop severely with increasing salt concentration (Fig. 3b).

## Conclusions

Systematic investigation of Li transport at the cathode-liquid electrolyte interface for electrolytes using two of the most commonly used salts, LiPF<sub>6</sub> and LiTFSI, has revealed exchange current

densities that are a factor of ~100 higher in electrolytes containing the TFSI<sup>-</sup> anion group compared to those containing PF<sub>6</sub><sup>-</sup> alone. When both anion groups are present, thereby competing to solvate Li<sup>+</sup> ions, the TFSI<sup>-</sup> group preferentially solvates Li<sup>+</sup>, yet results in a lower Li binding energy that provides for more facile desolvation and faster interfacial kinetics. For Li-ion cathodes with typical particle sizes in the range 5–30 μm, achieving high capacity at high current rates requires high exchange current densities comparable to those obtained herein using LiTFSI salt (2–3 mA cm<sup>-2</sup>). More broadly, these insights suggest a design approach and methodology for identifying electrolytes that can achieve improved performance at high current rates, as is increasingly desired for emerging transportation applications.

## Methods

**Materials and electrolytes.** NMC333 powders were obtained from TODA, Inc. Single NMC333 secondary particles within a narrow size distribution (28 ± 2 μm diameter) were physically isolated under an optical microscope from a source powder of broader size distribution, and attached to tungsten probes (Fig. 1) using a deposition and focused ion beam (FIB) etching procedure<sup>13</sup>. The tungsten probe (Tedpella Inc.) was coated with an insulating resin that suppressed the tungsten oxidation side reaction. A thin layer of platinum (Pt) was sputter-deposited where the cathode particle contacts the conductive probe, in the FIB. The single-particle NMC EIS and PITT measurements were conducted using a three-electrode cell (Supplementary Fig. 12).

Supplementary Table 1 summarizes the particle diameters of 16 single-particle electrodes and the corresponding electrolyte compositions in which the electrochemical measurements were carried out. The single-particle electrodes have a capacity of ~6 nAh (that is, ~1 billionth of a typical high capacity cellphone battery), and were tested against a lithium metal counter electrode with about 10<sup>3</sup> higher capacity (~70 mAh for foil of dimensions ~0.5 cm<sup>2</sup> × 720 μm thickness) to ensure that lithium transport kinetics at the counter electrode was not rate limiting. The three-electrode cell also has a large excess of liquid electrolyte (10 ml) so that the electrolyte composition is not affected during the measurement; the cell is also designed to avoid mass-transfer limitations<sup>13</sup>.

Cathode coatings of NMC333 (LiNi<sub>0.33</sub>Mn<sub>0.33</sub>Co<sub>0.33</sub>O<sub>2</sub>) on Al foil were kindly provided by Oak Ridge National Laboratory. These electrodes are composed of 90 wt% NMC333, 5 wt% carbon and 5 wt% PVDF, with ~30% porosity and 2 mAh cm<sup>-2</sup> area capacity (mass loading ~12.5 mg cm<sup>-2</sup>). The electrodes sheets were punched into discs and dried overnight at 105 °C under vacuum before using in electrochemical cells. For aluminium-free cells, ~200-nm-thick Pt coatings were deposited directly on stainless steel coin cell cases (MTI, CR2025) using a Q300TD sample preparation system (Quorum Technologies). NMC333 electrodes were prepared by mixing NMC333 (TODA Inc.) with carbon black and PVDF (Sigma-Aldrich, molecular weight ~400,000) in a weight ratio of 90:5:5 and slurries formed using N1-methyl-2-pyrrolidinone (NMP) (Sigma-Aldrich) as the solvent were cast onto the Pt-coated steel coin cell cases and dried under vacuum.

As-purchased bis(trifluoromethane)sulfonimide lithium salt (LiTFSI, 99.5%, Sigma-Aldrich) was first dried under vacuum at 108 °C for overnight in a glovebox (O<sub>2</sub> < 0.1 ppm, H<sub>2</sub>O < 0.1 ppm). Dimethyl carbonate (DMC, 99%, Sigma-Aldrich) solvent was dried using activated molecular sieves (3 Å, J.T. Baker) for over 1 week. Electrolytes containing LiTFSI salt were then mixed with a conventional 1 M LiPF<sub>6</sub> electrolyte (in DMC, battery-grade, Sigma-Aldrich) or in dried DMC alone in predetermined concentrations. Battery-grade electrolyte with 2 M LiPF<sub>6</sub> in DMC was also obtained from Sigma-Aldrich. Ionic conductivities of the electrolytes were calculated from the high frequency intercept of EIS impedance spectra measured in symmetric Pt|Pt Swagelok blocking cells at various temperatures (-10 to +30 °C), as shown in Supplementary Fig. 11.

**Cell set-up and electrochemical measurements.** Single-particle cell set-up and protocols to extract the kinetic parameters are given in Supplementary Methods and elsewhere<sup>13</sup>. An example of the Nyquist plots obtained from a single particle as a function of SOC is given in Supplementary Fig. 13. Numerical data obtained from EIS of individual particles are tabulated in Supplementary Tables 3–12, and from PITT measurements in Supplementary Tables 13–15. Charge/discharge performance of macroscopic composite electrodes were measured using CR2025 coin cells (Fig. 4a–c) or three-electrode Swagelok-type cells (Supplementary Fig. 4) with a VMP multichannel potentiostat (Bio-logic). NMC333 cathode was cast on Al foil with areal capacity of 2 mAh cm<sup>-2</sup> (~12.5 mg cm<sup>-2</sup>). Here, a 750-μm-thick Li foil anode (Aldrich) and 2500 separator from Celgard was used. Three formation cycles at 0.1 C (0.2 mA cm<sup>-2</sup>) were conducted before the higher charge/discharge-rate test. In the discharge-rate tests, all cells are charged at 1/3 C and held until the current decays below 0.1 mA, and discharged at increasing rates, and vice versa in charge-rate tests. The galvanostatic charge and discharge experiments were initially performed at current densities of 0.2 mA cm<sup>-2</sup>, which corresponds to approximately 1/10 C, and then of 1, 2, 4, 10 and 20 mA cm<sup>-2</sup> for 1/2, 1, 2, 5

and 10 C, respectively (1 C = 160 mA g<sup>-1</sup>). Cells were tested between 2.5 and 4.5 V except for the electrolyte containing 1 M LiTFSI only, in which the upper cutoff voltage was 4.15 V. Impedance spectra of three-electrode cells were taken over the frequency range 10<sup>-2</sup> to 10<sup>6</sup> Hz using Swagelok cells that incorporate a small amount of lithium metal as the reference electrode.

**Characterization.** XPS surface analysis was carried out using a Physical Electronics VersaProbe II scanning X-ray microprobe, which was outfitted with a monochromatic Al Kα X-ray source. To avoid exposure to air and moisture, samples were transported from the glovebox to the XPS instrument in a hermetically sealed container filled of Ar gas. Cells for XPS measurements were assembled using the electrode coatings described above and cycled at a current density of 0.2 mA cm<sup>-2</sup> for three formation cycles, followed by 2 mA cm<sup>-2</sup> for 20 cycles, then disassembled and rinsed with DMC for XPS analysis.

**MD simulations.** Classical MD simulations were performed on electrolytes with different Li salts and concentrations using the LAMMPS package<sup>31</sup>. The molecular mechanics force field was parametrized mainly from the general amber force field v.1.8, similar to a previous work on systems containing hexafluorophosphate (PF<sub>6</sub><sup>-</sup>)<sup>32,33</sup>. A cutoff distance of 1.2 nm was chosen for the Lennard-Jones interactions, and long-range electrostatic interactions were handled by the particle-mesh Ewald method<sup>34</sup>. Each simulation box contains 600 DMC molecules, and the appropriate amount of salt components (Li ions and anions) are added to achieve the desired molarity. For example, a salt/solvent ratio of 1:12 corresponds to an electrolyte with a 1 M concentration of LiPF<sub>6</sub>/LiTFSI. Each simulation box was created by randomly packing all molecules using Packmol in a sufficiently large cubic box with periodicity in all three directions<sup>35</sup>. A conjugated-gradient energy minimization was first performed on all simulation boxes. A time step of 0.5 fs was selected for MD simulations. Isothermal-isobaric ensemble simulations at room temperature were first performed for 2 ns to obtain the correct volumes of all systems. Subsequently, all systems were equilibrated at room temperature using canonical ensemble simulations for 5 ns. The simulations were then continued for another 10 ns and snapshots of the solvation structures were sampled at every 1 ps using the Python Materials Genomics (pymatgen) package<sup>36</sup>.

**DFT calculations.** The binding energies of the solvation structures at quantum mechanics level were calculated using the Gaussian 09 quantum chemistry package<sup>37</sup>. Given the large size of solvation structures (~60 atoms), geometry optimizations were only performed at the molecular mechanics level using the force field constructed for MD simulations. Single-point energy calculations at the B3LYP/6-311+G(2d,p) level were carried out after obtaining optimized geometries for all single molecules and solvation structures. The inclusion of diffuse functions in the basis sets ensures an adequate description of the diffuse electron cloud of anions. The dielectric constant of DMC (3.087) was applied in PCM calculations. The binding energies of solvation structure are calculated as:

$$E_{\text{bind}} = \sum E_{\text{molecule(sol)}} - E_{\text{cluster(sol)}} \quad (2)$$

where  $E_{\text{cluster(sol)}}$  is the energy of solvation structure and  $\sum E_{\text{molecule(sol)}}$  is the sum of energies of all molecules forming the solvation structure. For each type of cluster, 100 configurations sampled from MD snapshots were calculated.

## Data availability

All relevant data are included in the paper and its Supplementary Information.

Received: 1 August 2019; Accepted: 3 June 2020;

Published online: 29 June 2020

## References

- Fredericks, W. L., Sripad, S., Bower, G. C. & Viswanathan, V. Performance metrics required of next generation batteries to electrify vertical takeoff and landing (VTOL) aircraft. *ACS Energy Lett.* **3**, 2989–2994 (2018).
- Sander, J. S., Erb, R. M., Li, L., Gurijala, A. & Chiang, Y.-M. High-performance battery electrodes via magnetic templating. *Nat. Energy* **1**, 16099 (2016).
- Delattre, B. et al. Impact of pore tortuosity on electrode kinetics in lithium battery electrodes: study in directionally freeze-cast LiNi<sub>0.8</sub>Co<sub>0.15</sub>Al<sub>0.05</sub>O<sub>2</sub> (NCA). *J. Electrochem. Soc.* **165**, A388–A395 (2018).
- Suo, L. et al. “Water-in-salt” electrolyte enables high-voltage aqueous lithium-ion chemistries. *Science* **350**, 938–943 (2015).
- Yamada, Y. & Yamada, A. Review—superconcentrated electrolytes for lithium batteries. *J. Electrochem. Soc.* **162**, A2406–A2423 (2015).
- Yamada, Y. et al. Unusual stability of acetonitrile-based superconcentrated electrolytes for fast-charging lithium-ion batteries. *J. Am. Chem. Soc.* **136**, 5039–5046 (2014).
- Wang, J. et al. Superconcentrated electrolytes for a high-voltage lithium-ion battery. *Nat. Commun.* **7**, 12032 (2016).

8. Zheng, J. et al. Electrolyte additive enabled fast charging and stable cycling lithium metal batteries. *Nat. Energy* **2**, 17012 (2017).
9. Xu, K. Electrolytes and interphases in Li-ion batteries and beyond. *Chem. Rev.* **114**, 11503–11618 (2014).
10. Amin, R., Ravnsbæk, D. B. & Chiang, Y.-M. Characterization of electronic and ionic transport in Li<sub>1-x</sub>Ni<sub>0.8</sub>Co<sub>0.15</sub>Al<sub>0.05</sub>O<sub>2</sub> (NCA) batteries and energy storage. *J. Electrochem. Soc.* **162**, A1163–A1169 (2015).
11. Amin, R. & Chiang, Y.-M. Characterization of electronic and ionic transport in Li<sub>1-x</sub>Ni<sub>0.33</sub>Mn<sub>0.33</sub>Co<sub>0.33</sub>O<sub>2</sub> (NMC333) and Li<sub>1-x</sub>Ni<sub>0.50</sub>Mn<sub>0.20</sub>Co<sub>0.30</sub>O<sub>2</sub> (NMC523) as a function of Li content batteries and energy storage. *J. Electrochem. Soc.* **163**, A1512–A1517 (2016).
12. Jow, T. R., Delp, S. A., Allen, J. L., Jones, J.-P. & Smart, M. C. Factors limiting Li<sup>+</sup> charge transfer kinetics in Li-ion batteries. *J. Electrochem. Soc.* **2**, A361–A367 (2018).
13. Tsai, P.-C. et al. Single-particle measurements of electrochemical kinetics in NMC and NCA cathodes for Li-ion batteries. *Energy Environ. Sci.* **11**, 860–871 (2018).
14. Kanamura, K., Yamada, Y., Annaka, K., Nakata, N. & Munakata, H. Electrochemical evaluation of active materials for lithium ion batteries by one (single) particle measurement. *Electrochemistry* **84**, 759–765 (2016).
15. Ando, K. et al. Degradation analysis of LiNi<sub>0.8</sub>Co<sub>0.15</sub>Al<sub>0.05</sub>O<sub>2</sub> for cathode material of lithium-ion battery using single-particle measurement. *ACS Appl. Mater. Sci.* **1**, 4536–4544 (2018).
16. Li, J., Xiao, X., Yang, F., Verbrugge, M. W. & Cheng, Y.-T. Potentiostatic intermittent titration technique for electrodes governed by diffusion and interfacial reaction. *J. Phys. Chem. C* **116**, 1472–1478 (2012).
17. Li, J., Yang, F., Xiao, X., Verbrugge, M. W. & Cheng, Y.-T. Potentiostatic intermittent titration technique (PITT) for spherical particles with finite interfacial kinetics. *Electrochim. Acta* **75**, 56–61 (2012).
18. Inada, R., Kumasaka, R., Inabe, S., Tojo, T. & Sakurai, Y. Li<sup>+</sup> insertion/extraction properties for TiNb<sub>2</sub>O<sub>7</sub> single particle characterized by a particle-current collector integrated microelectrode. *J. Electrochem. Soc.* **33**, A5157–A5162 (2019).
19. Lin, F. et al. Surface reconstruction and chemical evolution of stoichiometric layered cathode materials for lithium-ion batteries. *Nat. Commun.* **5**, 3529 (2014).
20. Wang, F. et al. Hybrid aqueous/non-aqueous electrolyte for safe and high-energy Li-ion batteries. *Joule* **2**, 927–937 (2018).
21. Jiao, S. et al. Stable cycling of high-voltage lithium metal batteries in ether electrolytes. *Nat. Energy* **3**, 739–746 (2018).
22. Lu, Y.-C., Mansour, A. N., Yabuuchi, N. & Shao-Horn, Y. Probing the origin of enhanced stability of 'AlPO<sub>4</sub>' nanoparticle coated LiCoO<sub>2</sub> during cycling to high voltages: combined XRD and XPS Studies. *Chem. Mater.* **21**, 4408–4424 (2009).
23. Wagner, R. et al. Impact of selected LiPF<sub>6</sub> hydrolysis products on the high voltage stability of lithium-ion battery cells. *ACS Appl. Mater. Interfaces* **8**, 30871–30878 (2016).
24. Lebens-Higgins, Z. W. et al. Evolution of the electrode–electrolyte interface of LiNi<sub>0.8</sub>Co<sub>0.15</sub>Al<sub>0.05</sub>O<sub>2</sub> electrodes due to electrochemical and thermal stress. *Chem. Mater.* **30**, 958–969 (2018).
25. Sharova, V. et al. Comparative study of imide-based Li salts as electrolyte additives for Li-ion batteries. *J. Power Sources* **375**, 43–52 (2018).
26. Ensling, D., Stjerndahl, M., Nyttén, A., Gustafsson, T. & Thomas, J. O. A comparative XPS surface study of Li<sub>2</sub>FeSiO<sub>4</sub>/C cycled with LiTFSI- and LiPF<sub>6</sub>-based electrolytes. *J. Mater. Chem.* **19**, 82–88 (2009).
27. Quinlan, R. A., Lu, Y.-C., Shao-Horn, Y., Mansour, A. N. & Studies, X. P. S. Surface chemistry changes of LiNi<sub>0.5</sub>Mn<sub>0.5</sub>O<sub>2</sub> electrodes during high-voltage cycling. *J. Electrochem. Soc.* **160**, A669–A677 (2013).
28. Baggetto, L., Dudney, N. J. & Veith, G. M. Surface chemistry of metal oxide coated lithium manganese nickel oxide thin film cathodes studied by XPS. *Electrochim. Acta* **90**, 135–147 (2013).
29. Chapman, N., Borodin, O., Yoon, T., Nguyen, C. C. & Lucht, B. L. Spectroscopic and density functional theory characterization of common lithium salt solvates in carbonate electrolytes for lithium batteries. *J. Phys. Chem. C* **121**, 2135–2148 (2017).
30. Morita, M., Asai, Y., Yoshimoto, N., Ishikawa, M. & Raman, A. Spectroscopic study of organic electrolyte solutions based on binary solvent systems of ethylene carbonate with low viscosity solvents which dissolve different lithium salts. *J. Chem. Soc. Faraday Trans.* **94**, 3451–3456 (1998).
31. Plimpton, S. Fast parallel algorithms for short-range molecular dynamics. *J. Comput. Phys.* **117**, 1–19 (1995).
32. Wang, J., Wolf, R. M., Caldwell, J. W., Kollman, P. A. & Case, D. A. Development and testing of a general amber force field. *J. Comput. Chem.* **25**, 1157–1174 (2004).
33. Liu, Zhi, Huang, S. & Wang, W. A refined force field for molecular simulation of imidazolium-based ionic liquids. *J. Phys. Chem. B* **108**, 12978–12989 (2004).
34. Darden, T., York, D. & Pedersen, L. Particle mesh Ewald: an  $\mathcal{O}(N \log(N))$  method for Ewald sums in large systems. *J. Chem. Phys.* **98**, 10089–10092 (1993).
35. Martínez, L., Andrade, R., Birgin, E. G. & Martínez, J. M. PACKMOL: a package for building initial configurations for molecular dynamics simulations. *J. Comput. Chem.* **30**, 2157–2164 (2009).
36. Ong, S. P. et al. Python materials genomics (pymatgen): a robust, open-source python library for materials analysis. *Comp. Mater. Sci.* **68**, 314–319 (2013).
37. Frisch, M. J. et al. Gaussian (Gaussian, Inc., 2013).
38. Lee, C., Yang, W. & Parr, R. G. Development of the Colle-Salvetti correlation-energy formula into a functional of the electron density. *Phys. Rev. B* **37**, 785–789 (1988).

## Acknowledgements

This work was supported as part of the NorthEast Center for Chemical Energy Storage, an Energy Frontier Research Center funded by the US Department of Energy, Office of Science, Basic Energy Sciences under Award no. DE-SC0012583. Z.D. and S.P.O. acknowledge computational resources provided by the Triton Shared Computing Cluster at the University of California San Diego, and the Extreme Science and Engineering Discovery Environment supported by the National Science Foundation under grant no. ACI-1053575. Z. Du from Oak Ridge National Laboratory is acknowledged for kindly providing the casted NMC333 cathodes. Z.D. also acknowledges discussions with T. Hou, UC Berkeley, and help with MD from C. Jian, York University.

## Author contributions

B.W. and Y.-M.C. initiated and designed the research. B.W. conducted the experiments and electrochemical analysis. P.-C.T. assisted the nanofabrication with FIB. Z.D. and S.P.O. performed the MD simulations as well as DFT calculations. Z.W.L.-H. and L.F.J.P. assisted with XPS analysis. All authors contributed to writing the manuscript under the supervision of Y.-M.C.

## Competing interests

The authors declare no competing interests.

## Additional information

**Supplementary information** is available for this paper at <https://doi.org/10.1038/s41560-020-0647-0>.

**Correspondence and requests for materials** should be addressed to Y.-M.C.

**Reprints and permissions information** is available at [www.nature.com/reprints](http://www.nature.com/reprints).

**Publisher's note** Springer Nature remains neutral with regard to jurisdictional claims in published maps and institutional affiliations.

© The Author(s), under exclusive licence to Springer Nature Limited 2020